Submersed micropatterned structures control active nematic flow, topology, and concentration

Kristian Thijssen[a,b,1], Dimitrius A. Khaladj[c,1], S. Ali Aghvami[d,e], Mohamed Amine Gharbi[f], Seth Fraden[d], Julia M. Yeomans[a], Linda S. Hirst[c,2], and Tyler N. Shendruk[g,2]

[a]The Rudolf Peierls Centre for Theoretical Physics, Department of Physics, University of Oxford, Oxford OX1 3PU, United Kingdom; [b]Yusuf Hamied Department of Chemistry, University of Cambridge, Cambridge CB2 1EW, United Kingdom; [c]Department of Physics, University of California, Merced, CA 95343; [d]Physics Department, Brandeis University, Waltham, MA 02453; [e]Department of Molecular Metabolism, Harvard University, Boston, MA 02115; [f]Department of Physics, University of Massachusetts, Boston, MA 02125; and [g]School of Physics and Astronomy, The University of Edinburgh, Edinburgh EH9 3FD, United Kingdom

Coupling between flows and material properties imbues rheological matter with its wide-ranging applicability, hence the excitement for harnessing the rheology of active fluids for which internal structure and continuous energy injection lead to spontaneous flows and complex, out-of-equilibrium dynamics. We propose and demonstrate a convenient, highly tunable method for controlling flow, topology, and composition within active films. Our approach establishes rheological coupling via the indirect presence of fully submersed micropatterned structures within a thin, underlying oil layer. Simulations reveal that micropatterned structures produce effective virtual boundaries within the superjacent active nematic film due to differences in viscous dissipation as a function of depth. This accessible method of applying position-dependent, effective dissipation to the active films presents a nonintrusive pathway for engineering active microfluidic systems.

active matter | micropatterned control | topological defects | nematic film | active depletion

Active fluids are inherently out of equilibrium; they locally transform internal energy into material stresses that can result in spontaneous hydrodynamic motion. An increasing number of biophysical systems, including colonies of bacilliform microbes (1–4), cellular monolayers (5–9), and subcellular filaments (10–12), display such collective active motion, orientational order, and topological singularities. Controlling active dynamics is essential not only to fully understanding how such biological systems employ self-generated stresses but also, in order to develop active microfluidic devices.

To this end, recent work considers how confining walls (13–15), arrangements of obstacles (16, 17), and the dynamics of topological defects (18) dictate active nematic flow. Control of active material concentration has been studied from the perspectives of coexistence of phases in self-propelled rods (19–21) and motility-induced phase separation (22–24). Controlled accumulation and depletion of active matter have been engineered in bacterial systems to concentrate cells (25, 26) and to drive bacterial-ratchet motors (27–29). Similarly, substrate gradients modify cellular motility, driving density variation (30) and directed migration (31, 32).

In addition to varying concentration and flow, topology has been controlled by including externally driven flows (33–35) and curvature (36, 37). Recent work shows that locally altering activity modifies defect populations (38–41), and anisotropic smectic sublayers below active nematic sheets can constrain orientation (42). Such studies demonstrate how underlying sublayer properties have pronounced effects on active dynamics and suggest approaches for engineering control of active matter.

We propose a micropattern-based method for controlling active nematic dynamics without contiguous contact with active films. By patterning oil-submersed solid substrates below two-dimensional (2D) active nematic films with geometrical structures of differing height, we achieve effective virtual boundaries within active films that control topological defect populations, collective flow, and concentration of active nematic material without penetrating the film. By implementing underlying submersed patterned microstructures, we tune the depth of the oil layer to adjust dissipation within the superjacent film and thereby, generate a highly tunable technique for controlling the active dynamics. Presently, we introduce four initial submersed structures: micropatterned trenches (Fig. 1 *A–C*), undulated substrates (*SI Appendix*, Fig. S1), stairways (Fig. 1 *D–F*), and pillars (Fig. 1 *G–I*).

Trench

To investigate how structures fully submersed in a layer of oil influence defect dynamics in the superjacent active film, we consider the trench geometry depicted in Fig. 1*A*. An active nematic microtubule network is generated at an oil–water interface above a micropatterned trench of depth $\Delta_t = 18 \pm 1$ μm and width $w_t = 327 \pm 2$ μm fabricated using photolithography (*Materials and Methods*). We observe that flows in the active nematic layer

Significance

Methods to manipulate and control the dynamics of spontaneously flowing active materials are vital if these fluids are to lead to technological applications. We report the development of an easy-to-implement technique to achieve tunable, local control over active nematic films, the preeminent example of active fluids. We establish that micropatterns, fully submersed below active films, have a pronounced impact on dynamics. To showcase the adaptability of our technique, we present four proof-of-concept microstructures: trenches, undulated sinusoids, stairways, and pillars. Each illustrates a particular strength of our approach, including enacting abrupt virtual boundaries to trap topological defects, separating distinct flow states at constant levels of biochemical fuel, gently guiding self-propelled defects, and modifying local active nematic composition.
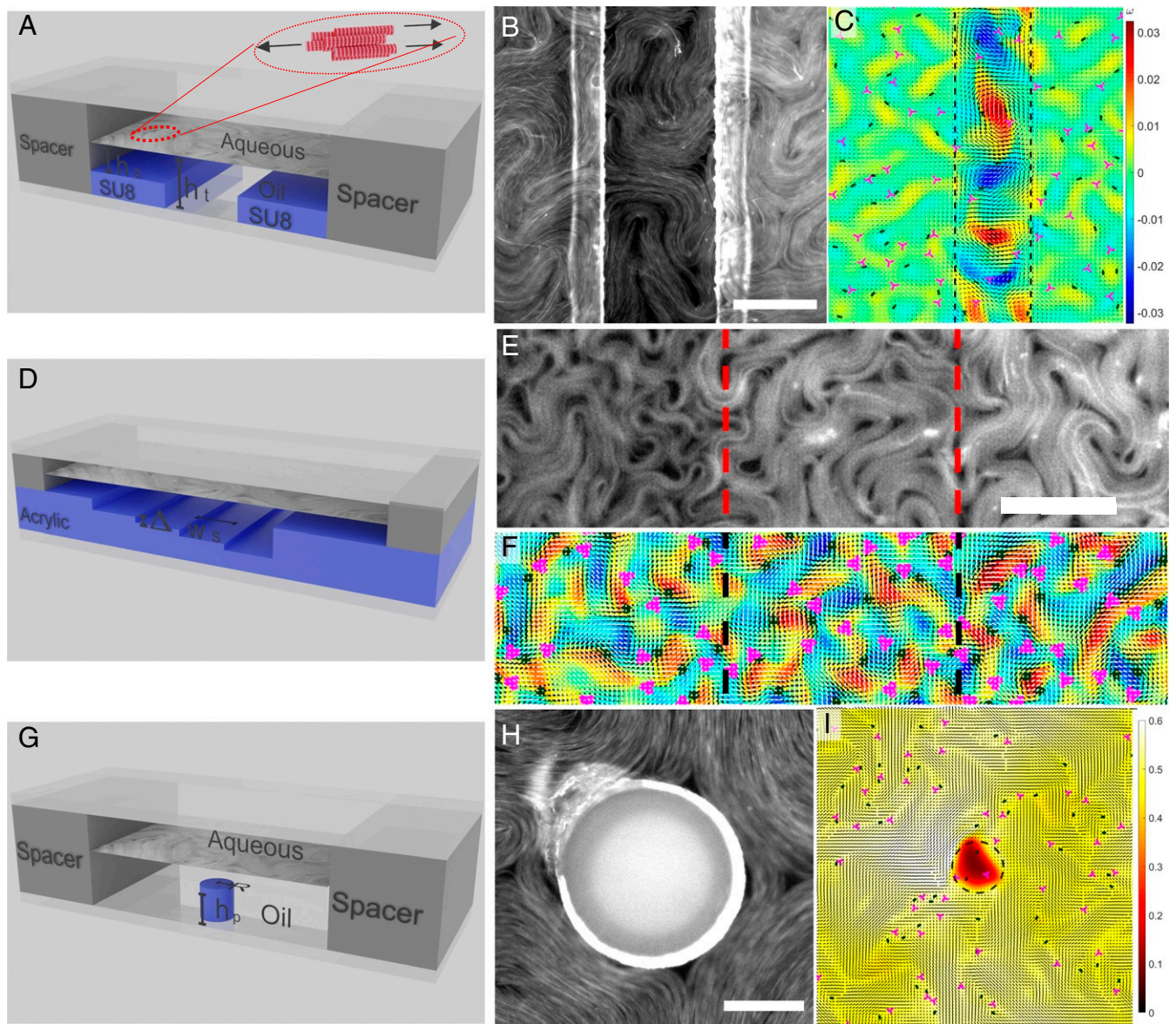
PHYSICS

Fig. 1. Submersed micropatterns control active nematic dynamics. (*A–C*) Trench setup. An active film resides at the oil–water interface above different substrate depths. The active flows drag the underlying oil layer, but viscous dissipation is depth dependent, affecting active nematic film dynamics. (*B*) Fluorescence microscope image of the active nematic bundled microtubule film above a submersed trench. (Scale bar: 250 μm.) (*C*) Simulation results for the vorticity field within the superjacent active nematic layer. The flow behaviors within the low-friction region (between the dashed lines) are distinct from the behavior in the high friction region (beyond the dashed lines). Plus-half (minus-half) defects denoted by dark green (magenta) symbols behave differently in the two regions. (*D–F*) Stairway setup. (*E*) Fluorescence microscope image of the micromilled stairway and the superjacent bundled microtubule film. Step location is indicated by dashed lines. The oil depth increases from left to right. The differences in oil depth alter the length scale of the active turbulence above each step. (Scale bar: 250 μm.) (*F*) Simulations results for discrete steps in the effective friction (dashed lines). The effective friction coefficient decreases from left to right. The color bar is shared with *C*. (*G–I*) Pillar setup. (*H*) Fluorescence microscope image of the bundled microtubule film above the SU-8 micropillar. (Scale bar: 100 μm.) (*I*) Simulation results show that the active nematic concentration ϕ is depleted within the high-friction region encircled by the pillar perimeter (dashed line).

exhibit coexistence of two distinct regions: one directly above the trench and another in the shallows surrounding the trench (Fig. 1*B*). These regions are separated by well-defined virtual boundary lines located directly above the trench edges. The trench edges are visible as a pair of parallel white lines due to stress-induced autofluorescence of the micropatterned photoresist in regions of precipitous height change. Beyond the trench boundaries, the active nematic retains the chaotic nature of active turbulence; however, within the boundaries, the trench width establishes a local confining length scale within the superjacent active nematic film (Movie S1). These virtual walls trap defects in

the trench region and produce active flow behaviors comparable with those observed in confining channels (14, 43–46). This result illustrates how such effective virtual boundaries can be used to define areas of orderly flows and areas of active turbulence without penetrating the active film.

The $\pm 1/2$ topological defect distributions across the trench (*Materials and Methods*) demonstrate that $-1/2$ defects tend to be located in the vicinity of the virtual boundary (Fig. 2*A*). Experimental observations of $-1/2$ defect trajectories near the boundary reveal that they tend to linger over long intervals, contributing to peaks (Movie S1). In contrast, $+1/2$ defects
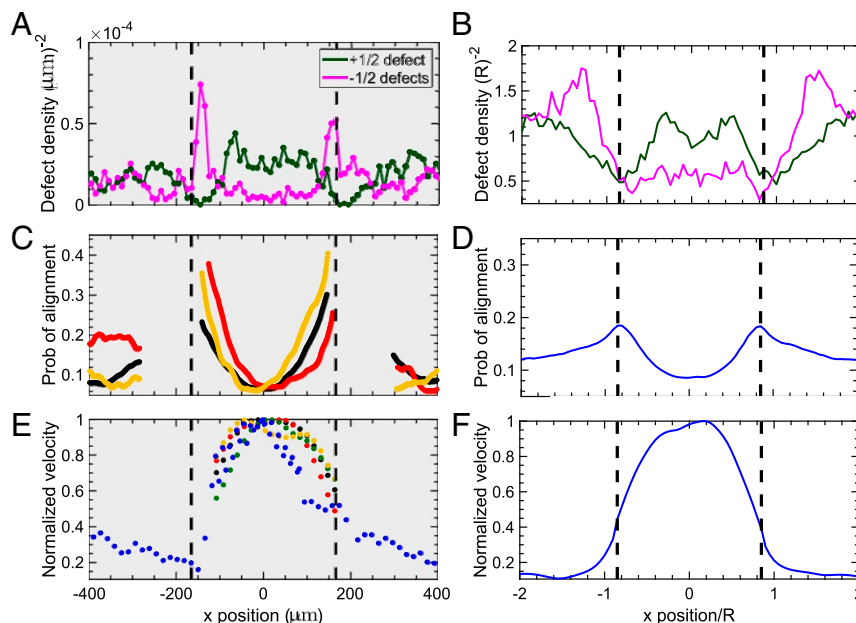
Fig. 2. Positive defects depleted at the trench interface. *A, C,* and *E* show experimental results, while *B, D,* and *F* show numerical results. (*A* and *B*) Distribution of $+1/2$ (dark green) and $-1/2$ (magenta) defects as a function of transverse position *x* measured from experiments and simulations, respectively. (*C* and *D*) The probability profile that the nematic director is oriented less than $10°$ from the direction parallel to the trench wall as a function of *x*. The director field has a high probability of alignment with the virtual boundary. The gap in data at the trench edge is explained in *Materials and Methods*. (*E* and *F*) Normalized rms fluid velocity profile across the trench. Experimental results in *E* are calculated from two different identical trenches. The experimentally measured maxima are $\{4.00, 1.68, 1.57, 1.00, 1.12\}$ $\mu m/s$. Colors in *C* and *E* denote different experimental iterations.

tend to be depleted from the vicinity of the trench boundary and are confined within the trench region, moving along oscillatory trajectories that do not typically approach the boundaries (Movie S1). In the exterior region, far from the virtual trench, the defect density profile approaches a homogeneous distribution of positive and negative defects.

The effective virtual boundaries arise from abrupt steps in fluid depth $h(\boldsymbol{r})$ between the film and the underlying substrate at each point $\boldsymbol{r}$. The fluid depth h increases from h_s in the surrounding shallows to a trench depth $h_t = h_s + \Delta_t$ (Fig. 1*A*). As activity drives flows within the nematic film, the underlying oil layer viscously dissipates momentum due to the subjacent no-slip substrate, which can be described as a local effective friction $\gamma(\boldsymbol{r})$ acting on each point within the superjacent active film (47). Following from the lubrication limit, the effective friction coefficient scales as $\gamma \sim \eta'/h(\boldsymbol{r})$, where η' is an effective viscosity of the film and surrounding fluids. The abrupt height change across the trench boundaries results in sharp, virtual boundaries.

We replicate the observed experimental phenomena with 2D active nemato-hydrodynamic simulations, in which the submersed micropatterns are incorporated via an effective friction field (*Materials and Methods*). Numerical results demonstrate that a step in effective friction can reproduce the experimentally observed active flows (Fig. 1*C*) and introduce virtual boundaries in the active layer, which repel $+1/2$ defects (Fig. 2 *A* and *B*). Integrating the defect density across the channel in Fig. 2*B* gives net zero charge; however, it is more challenging to accurately identify minus defects than positive in experiments. As a result, this labeling bias causes a slight net positive charge in Fig. 2*A*. The qualitative agreement in behavior between experimental and numerical defect distributions demonstrates how effective friction is the mechanism by which micropatterned structures create virtual planar boundaries and introduce a confinement length scale to the active nematic without penetrating the film. The $-1/2$ defect density peak at the virtual boundary (Fig. 2*A*) is consistent with work (14, 46) showing that walls can act as

catalysts for pair creation and unbinding; while newly created $+1/2$ defects move away due to self-propulsion, the $-1/2$ defects remain near the boundary.

While the experimental $-1/2$ defect density peaks sharply in the vicinity of the virtual boundaries (Fig. 2*A*), it is broadened and peaked outside the trench region in simulations (Fig. 2*B*). To understand this difference, we consider the time-averaged director orientation across the trench (Fig. 2*C* and *Materials and Methods*), which reveals that the virtual boundaries introduce an effective alignment of the director as the probability of aligning to the interface becomes different from the bulk, similar to that seen for impermeable boundaries (14, 46). This is because any orthogonal bundle midway over the boundary is subject to a large axial laminar flow inside and slow disorderly flows outside, which compete to produce an aligning torque. The model captures this behavior, showing that the probability declines to a uniform distribution far from the trench (Fig. 2*D*). Experiments exhibit stronger planar alignment at the virtual boundaries than simulations. This is likely related to the model's assumption of a continuous fluid (*Materials and Methods*), which is in contrast to the network of finite-sized microtubule bundles that act as material lines preventing defects from crossing (14), resulting in an accumulation. This is reminiscent of simulation studies of passive nematic tactoids where defects travel outside the interface and become virtual unless an anchoring term is included (48). Future research is needed to more fully understand if an effective term can be devised to account for this effect in continuum models that do not contain sharp ϕ interfaces. The stronger alignment in the experiments constrains the $-1/2$ defects to the region inside the trench, while in simulations, they are pushed to the outside of the boundaries (Fig. 2 *A* and *B*). In both experiments and simulations, $+1/2$ defects are trapped between the virtual boundaries.

The submersed trench not only impacts the nematic field but also, generates a virtual boundary for the velocity field (Fig. 2 *E* and *F*). Superjacent to the trench, velocities are lower in the

Thijssen et al.
Submersed micropatterned structures control active nematic flow, topology, and concentration

PNAS | 3 of 10
https://doi.org/10.1073/pnas.2106038118

proximity of the trench boundary and maximum at the trench center. Since activity varies slightly between experimental realizations, we normalize the flow profiles (Fig. 2E) and compare with the decrease predicted by the model (Fig. 2F). The virtual boundaries do not impose no-slip conditions but decrease the speed to the slower value of the surrounding active turbulence, which can be seen explicitly for an experimental instance (blue dots in Fig. 2E) and in simulations (Fig. 2F). The decreasing flow profile explains the preferential alignment of the microtubule bundles in the vicinity of the virtual boundaries (Fig. 2 C and D). Any orthogonal bundle midway over the boundary is subject to a large axial, laminar flow inside and slow disorderly flows outside, which compete to produce an aligning torque.

Comparing the faster flow profile above the trench with the slower, disorderly active turbulence in the exterior region calls attention to the fact that active turbulence is a low–Reynolds number phenomenon (49). Confinement screens chaotic flows that would otherwise develop on scales larger than the trench width, while the low friction allows the rapid but steady flow profiles superjacent to the trench (Fig. 1 B and C). On the other hand, the higher friction produces a smaller characteris-

tic length scale (50) but also, slower speeds in the shallows. Thus, the submersed micropatterned trench segregates rapid laminar flow above the trench and slow but disorderly active turbulence outside.

Because the submersed micropatterned trench produces virtual boundaries that introduce a confining length scale, the competition between confinement and intrinsic active nematic length scale can be probed. Fig. 3A and Movie S1 experimentally demonstrate that a recurrent vorticity structure is established between the virtual boundaries when active and confining scales coincide (14, 17, 43), and simulations underscore the periodicity of counterrotating vortices (Fig. 3B and Movie S2). Examining the velocity autocorrelation functions quantifies the different flow profiles above the trench (Fig. 3 E and F, blue curve). The correlation function exhibits repetition between correlated and anticorrelated regions due to repeating clockwise and anticlockwise vortices. Active turbulence exists outside of the virtual channel, as characterized by an immediate initial drop in the correlation (Fig. 3F, dashed curve).

In narrower or wider confinements, the flow transitions to other states (Fig. 3 C–F). In simulations of the narrow trench
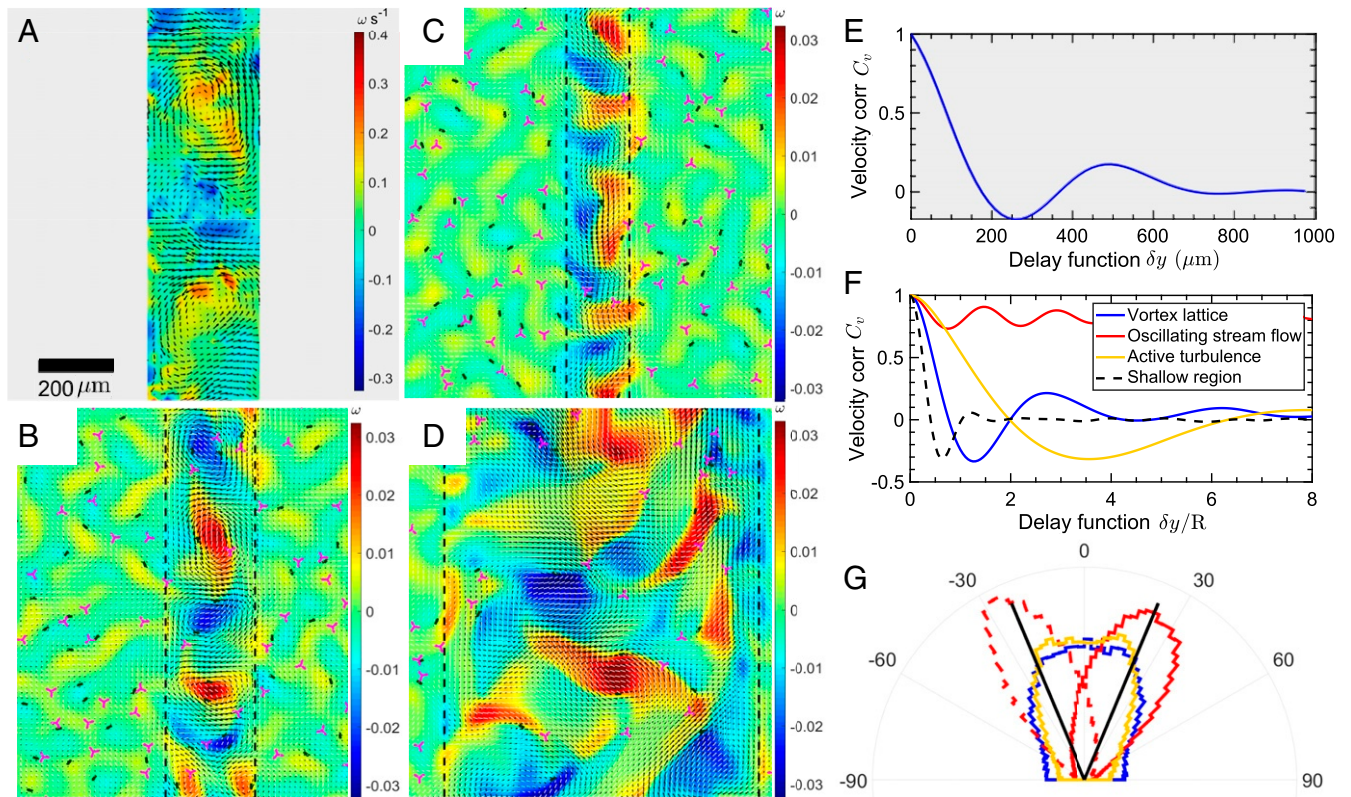

Fig. 3. Friction boundaries result in separate flow regions. (A) Instantaneous experimental vorticity superjacent to the deep trench region from particle image velocimetry (PIV) for a trench of width $w_t = 325$ μm. A and E show experimental results, while B–D, F, and G show numerical results. (B) Simulation snapshot of a repeating lattice of counterrotating vortices above a trench of width $w_t = 1.7R$ (Materials and Methods). Plus-half defects (dark green) are trapped between the virtual boundaries, generating the repeating vortex structure along the center line that is distinct from the active turbulence that exists outside the virtual boundaries. (C) Decreasing the trench width to $w_t = 1.2R$ in simulations results in long-range, oscillatory, streaming flow inside the trench. (D) Increasing the trench width to $w_t = 6R$ in simulations results in active turbulence both inside and outside the trench region but with differing intrinsic length scales due to the different effective frictions. (E) The velocity–velocity autocorrelation function $C_v(\delta y) = \langle \mathbf{v}(\mathbf{r}; t) \cdot \mathbf{v}(\mathbf{r} + \delta y\, \hat{\mathbf{y}}; t) \rangle / \langle v^2 \rangle$ for the experiment illustrated in A measured a distance δy along the $x = 0$ center line of the trench. Due to the confinement effect, long-range flow structures are formed in the low-friction regime epitomized by the strong correlation–anticorrelation–correlation signal. (F) Autocorrelation functions calculated from the simulations inside the channel shown in B (blue), C (red), and D (yellow), and the shallow region outside the virtual channel (dashed). The blue curve displays pronounced correlation and anticorrelation indicating the counterrotating vortex pattern in B, which corresponds to the behavior observed in the presented experiments of A and E. The red curve is long lived and fully correlated in the narrow channels of C, while the yellow curve decorrelates to zero after an anticorrelation, signaling active turbulent behavior both within and outside the virtual boundaries. (G) The director angle probability density at the friction boundaries of B–D. The solid (dashed) lines correspond to measurements at the right (left) friction boundary. The black lines are the analytical Leslie angles ($\theta_L = 22°$).

(Fig. 3C), the flows are long ranged and oscillatory with a preference for aligning with the boundaries (Fig. 3F). This oscillatory-streaming state occurs when the confining length scale w_t is small compared with the low-friction intrinsic active nematic length scale (43). Increasing the trench width predicts active turbulence in both the area superjacent to the trench and the shallow exterior regions (Fig. 3D) but with differing active nematic length scales (Fig. 3F). Equivalently higher levels of activity decrease the active length scale, and we have experimentally observed instances of disorderly flow states in both regions. The structure of the different flow states impacts the effective director alignment observed in Fig. 2D. For streaming flow that is dominated by a simple shearing flow with small fluctuations, we find the most likely angle the director makes with the virtual boundary, as seen in Fig. 3G. These angles are distributed about the Leslie angle $\theta_L = 22°$ (Materials and Methods), furthering our argument that the preferred orientation is due to flow alignment. In the wider trenches, the director varies widely due to defect creation events (46), but we still see a symmetry breaking as perpendicular alignment to the interface is disfavored due to the aligning torque. The relative position of the $-1/2$ defect peak to the interface does not change as we alter the trench width.

The trench geometry demonstrates that submersed microstructure patterning can impose confining virtual boundaries and is a feasible technique for maintaining coexistence of distinct flow behaviors simultaneously at different locations in a single active nematic layer. A strength of our submersed, micropatterned structure approach is that the boundaries act without physically penetrating the film, and so, active material does not first have to saturate a cavity before confinement dynamics can be explored (14). Filling complex geometries with filament-based active material may be the prohibitive step in active microfluidics (51). The proposed micropatterned method circumvents these difficulties, opening possibilities for experiments involving more complex geometries and fine-tuned positional control.

Sinusoid Substrates

While the trench geometry demonstrates that micropatterns with precipitous edges can actualize abrupt boundaries within superjacent active films, the ability to gradually tune the effective friction through gradients in oil-layer thickness allows our technique to gently guide defect dynamics. To demonstrate this, an undulating effective friction is produced by fully submersing a micropatterned one-dimensional sinusoidal substrate (Materials and Methods) characterized by amplitude $\Delta_u = 40 \pm 2$ μm and wavelength $\lambda_u = 150 \pm 2$ μm. Unlike the trench geometry, the sinusoid system does not separate into distinct coexisting flow states (Movie S3). Rather, the resulting anisotropic friction gradients present a means of orientation control of motile defects. Self-propelled $+1/2$ defects orient and travel in trains above the troughs (SI Appendix, Fig. S1A). Motile defects move through the system subject to friction gradients when they have components perpendicular to the troughs, such that trajectories coaligned with the troughs minimize dissipation, causing the observed parallel/antiparallel laning of $+1/2$ defects. Similar trains have been observed in active nematic layers above smectics (52), but since the spacing between smectic layers is significantly smaller, the defect trains in that configuration are not caused by gradients in effective friction; rather, they are due to uniform anisotropic friction.

However, such trains of $+1/2$ defects do not persist indefinitely since the trains produce nematically ordered regions, which are susceptible to the extensile-active nematic hydrodynamic bend instability (53–55), causing pair creation events that inevitably destabilize the flow (Movie S3). Since initially unbound $+1/2$ defects are typically oriented perpendicular to

the nematic ordered lanes (SI Appendix, Fig. S1B), this produces a cross-hatched trajectory pattern. These dynamics are not nearly as pronounced in sinusoid systems with a larger wavelength ($\lambda_u = 500$ μm) (Movie S4). Positive defects that are partially oriented along the friction gradient exhibit the same deflected motion as in the smaller wavelength system; so, the motile defects show some alignment along the troughs, but the cross-hatched dynamics are indiscernible. The sinusoid geometry demonstrates that submersed micropatterned structures can fine tune the active flow and nematic structure, thereby offering a means to guide and control defect dynamics.

Stairs

We now present a substrate patterned as a submersed stairway (Fig. 1D) designed to simultaneously observe active turbulence and gradations in the characteristic length scales (Movie S5). Individual steps are micromilled to possess horizontal width $w_s = 500 \pm 2$ μm and height of $\Delta_s = 10 \pm 1$ μm (Materials and Methods). The fluid depth is $h(\mathbf{r}) = h_0 + \Delta_s n(x)$, for step number n and initial fluid depth $h_0 = 12 \pm 3$ μm, determined through confocal microscopy (Materials and Methods and SI Appendix, Fig. S2). We focus on steps $7 \leq n \leq 9$ for which the microtubule network forms a well-defined continuous nematic field (Fig. 1E and Movie S5). As the depth increases with n, the effective dissipation within the oil layer decreases, which we simulate via discrete steps in effective friction in the superjacent active film (Fig. 1F and Materials and Methods).

Above the step pattern, the active length scales increase with decreasing friction, as characterized by the defect distribution (Figs. 1 E and F and 4A and Movie S5). Within each step, the
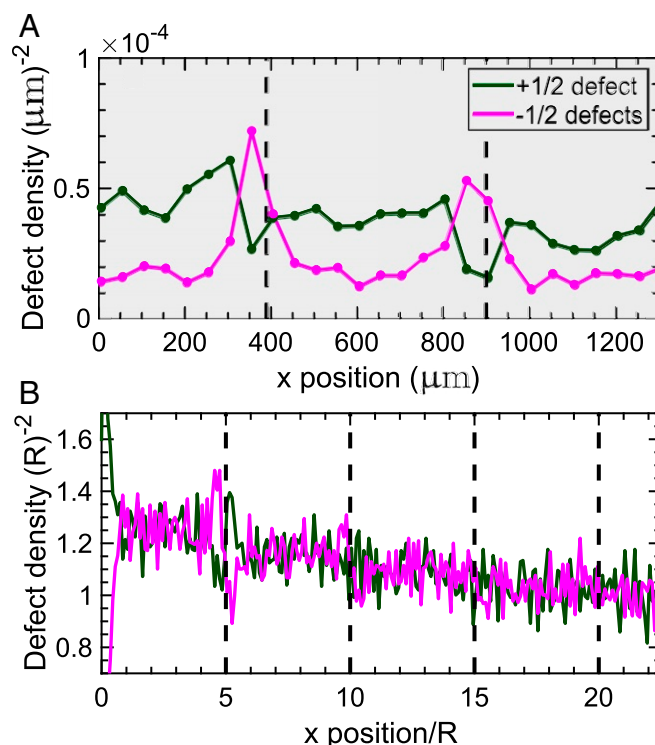
Fig. 4. The submersed micropatterned stairway allows simultaneous coexistence of regions of separated active turbulence with differing defect densities, while ATP concentration remains constant. Plus-half (dark green) and minus-half (magenta) defect distribution as a function of the position down the stairway x. (A) Measurements from experiments for steps of width $w_t = 500$ μm (gray shaded background). (B) Measurements from simulations for steps of width $w_t = 5R$.

Thijssen et al.
Submersed micropatterned structures control active nematic flow, topology, and concentration

PNAS | 5 of 10
https://doi.org/10.1073/pnas.2106038118

distribution is flat. However, at each edge, the number density of $-1/2$ defects peaks, while the density of $+1/2$ defects plunges. This is consistent with defect densities at the edges of the trench (Fig. 2 *A* and *B*). Although the simulated defect peaks are less pronounced than in experiments, numerical results show more clearly the decrease in defect density across multiple steps. The change in defect density is modest, consistent with studies demonstrating that increasing oil viscosity five orders of magnitude only increases defect density by a factor of order unity (56, 57), which highlights the potential tunability of our method. Because the effective friction is inversely proportional to oil depth, changes to the defect density become less pronounced with step number, and in the large oil-depth limit, substrate features become indiscernible within the nematic flows.

Interestingly, we only observe a continuously well-defined nematic field for oil depths that are much greater than h_0 in both experiments and simulations (Fig. 1*E*). We could reliably resolve the nematic order and measure defect density with low experimental uncertainty for steps $n \geq 7$. For small n, the active film exhibits disorderly nonhomogeneous textures akin to those observed in experiments utilizing high-viscosity oils (56). This suggests that submersed micropatterned structures can do more than impact flow and orientational state; we now demonstrate how substrate micropatterning can be used to control active matter concentration via structures raised above the solid substrate yet still fully submersed in the underlying oil layer.

Pillars

We consider fully submersed SU-8 pillar structures (Fig. 1*G*) of radius $r_p = 116 \pm 2$ μm and height $h_p = 6.8 \pm 0.3$ μm. As in the trench, sinusoid, and stairway geometries, the active nematic layer is subject to a step change in the effective film friction. However, differentiating it from previous structures, the pillar's virtual boundary forms a closed loop. The most prominent effect is a pronounced dilution of active material from the enclosed region above the pillar (Fig. 1*H* and Movie S6), which is qualitatively recapitulated in the simulations (Fig. 1*I*, *Materials and Methods*, and Movie S7). The phase-field active material concentration $\phi(\boldsymbol{r}; t)$ (*Materials and Methods*) demixes in the high–effective friction region directly above the pillar. We confirm that the absence of active material is not a result of the pillar intruding through the active nematic film by occasionally observing microtubule bundles moving above the apex of the pillar (Movie S8). Further, we did not observe curvature of the superjacent active layer in the vicinity of the micropillar, indicating that a finite oil depth lies between the subjacent pillar top and the nematic film.

To understand the mechanism leading to the pillar-bound dilute phase of active matter, we consider a simplified model of the active nematic. The effective friction is locally large above the pillar, causing the flow speed to decrease in the enclosed area but remain nonzero beyond the pillar border (Fig. 5*A*). Since nematic ordering arises in active microtubule network films due to activity-induced motion, the sharp decrease in flow causes a corresponding drop in nematic scalar order S across the circular virtual border (Fig. 5*B*). However, the abrupt gradient in S produces a radially outward average active force $\boldsymbol{\bar{f}}(r; t) \sim \langle \boldsymbol{\nabla} \cdot \mathbf{Q}(\boldsymbol{r}; t) \rangle \approx \partial_r \zeta(r; t) S(r; t) \hat{\boldsymbol{r}}$ (Eq. **6** in *Materials and Methods*), when the variation of the nematic order is dominated by the radial change in scalar order parameter and bend-induced stresses are neglected. Thus, the active forcing is expected to be radially outward and sharply peaked about the interface as observed in simulations (Fig. 5*C*). Interestingly, this argument suggests that contractile systems still deplete from the pillar region. While the ζ term will change sign, so will the $\partial_r S(r; t) \hat{\boldsymbol{r}}$ since contractile flows lower the nematic order (58). This is observed in simulations (*SI Appendix*, Fig. S3).

However, activity does not simply produce increased pressure across the perimeter but rather, is able to selectively deplete the concentration of active material ϕ, which enables depletion in incompressible films. Since the active film is considered incompressible, fluid mass density is constant, and hence, divergence of the film velocity is zero (Eq. **3** in *Materials and Methods*). Thus, for depletion to occur, it is demanded that outward advection is more frequent in regions where ϕ is larger on average. This is indeed the case because the activity depends on the local amount of active material present, $\zeta(r; t) = \zeta_0 \phi(r; t)$ (Eq. **7** in *Materials and Methods*), which causes the radially outward forcing to be stronger in magnitude where ϕ is large. For this reason, if the surrounding active turbulence stochastically advects ϕ-rich active material across the perimeter, the local active forces increase in kind. Hence, the active forces selectively repulse the material from the dissipative region (Fig. 5*D* and Movie S7). However, the local active forces decrease when ϕ-poor fluid enters. This allows the concentration to more easily cross the perimeter. In this way, the depletion of active matter above the pillar is a result of the high effective friction lowering the velocity. This causes nematic discomposure and selectivity due to the direct dependence of activity on the local concentration (Fig. 5*E*).

Noting that the highest steps in the stairway geometry also fail to exhibit continuous nematic fields but are not devoid of active matter (Fig. 1*D* and Movie S5), we test if the curvature of the virtual barriers impacts depletion by simulating a rectangular pillar (*SI Appendix*, Fig. S4). We observe a comparable depletion of ϕ from the enclosed area as in the circular pillar and so, conclude that curvature is not the critical difference. Second, we consider a circular pit where the friction is zero for radius $r < R$ and $\gamma = 0.1$ for $r > R$. We find that the active forces point inward and observe an accumulation of ϕ (*SI Appendix*, Fig. S5). These inward active forces can even be used to trap two $+1/2$ defects for small radii, resulting in circulatory motion reminiscent of an active nematic in circular confinement (*SI Appendix*, Fig. S6) (14).

We conclude that accumulation or depletion of active material using submersed micropatterned structures relies principally on two attributes. 1) The oil layer must be thin (high effective friction) to suppress the active flows necessary to exhibit nematic order. 2) An enclosed area must be circumscribed by a virtual boundary to prohibit longitudinal active streams through the incompressibility constraint. Hence, we only find minute changes in ϕ to occur in the trench and stair geometries. Lastly, we point out that material does not deplete from the pillar center in simulations on timescales investigated when a pillar radius is much larger since the material does not diffuse to the interface where it could be selectively depleted.

In addition to controlling concentration, submersed pillars interact with defects. We observe a greater frequency of $-1/2$ defects in the vicinity of the virtual boundary in our simulations (Fig. 5 *F* and *G*). The planar alignment of the director field explains the distribution of defects at the pillar boundary (Fig. 1 *H* and *I*). The resulting bend deformation around the perimeter drives hydrodynamic instabilities to continually generate defect pairs, with newly created self-motile $+1/2$ defects typically oriented radially away from the center such that they swiftly move away from the interface (Movie S9), leaving unbound immotile $-1/2$ defects behind (Fig. 5 *F* and *G*).

Submersed pillars can also serve as a virtual obstacle for defect trajectories (Movie S9). Positive defects that approach the pillars from the surrounding turbulence stall or are deflected when in proximity to the pillar (Fig. 5 *H–J*). In Fig. 5 *H* and *J*, we exhibit 9 representative trajectories of the 38 analyzed, and we show 4 from a total of 360 in Fig. 5*I* to illustrate the observed interactions. Deflected $+1/2$ defects first slow as they approach the pillar, then scatter, and regain speed as they move away from the submersed structure (Fig. 5 *H* and *I*). Positive defects that stall
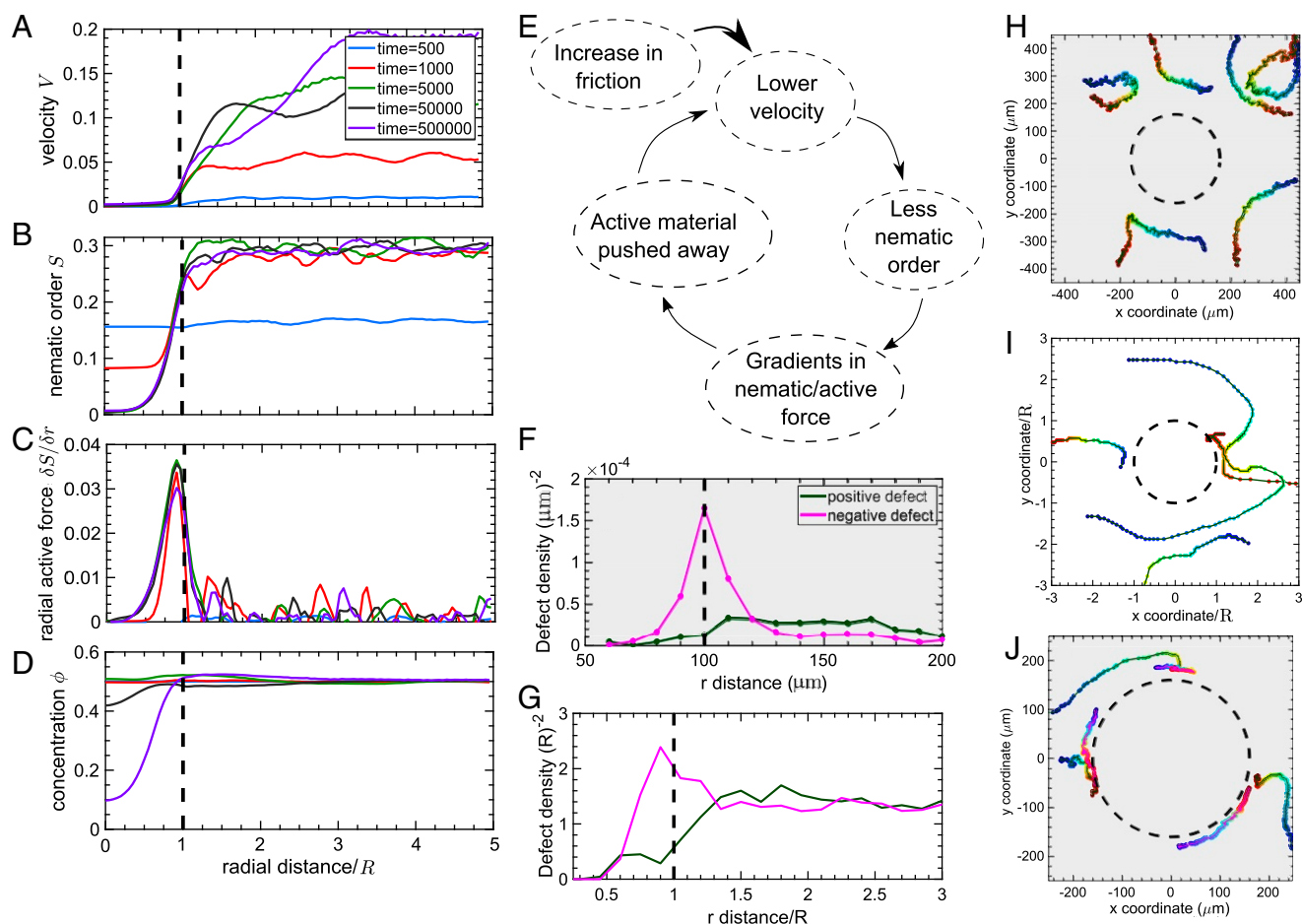
Fig. 5. Pillars cause local high-friction regions, which result in active matter depletion. (*A*) Due to the higher friction, the flow in the active nematic film remains low. (*B*) The nematic is highly ordered far from the pillar but disordered above it because the speed is lower in the higher-friction region. (*C*) The difference in nematic order at the friction interface results in a radial active force. (*D*) This radial active force pushes the active material concentration outward, resulting in depletion effects. *A–E*, *G*, and *I* show numerical results, while *F*, *H*, and *J* show experimental measurements. (*E*) The schematic of *A–D*. (*F* and *G*) +1/2 (dark green) and −1/2 (magenta) defect distributions as a function of radial distance from a submersed pillar from experiments (*F*) and simulations (*G*). Dark green and magenta lines denote +1/2 and −1/2 defects, respectively. (*H–J*) The *xy* trajectories of example ±1/2 defect dynamics in the vicinity of the pillar. Time along the trajectory is displayed as circular markers colored blue at the initial time and changing to red at the final instant. (*H* and *I*) +1/2 defects deflecting from the pillar: experiments (*H*) and simulations (*I*). (*J*) Experimental *xy* trajectories of +1/2 defects absorbing to the pillar boundary through defect annihilation with −1/2 residing in the vicinity of the perimeter.

as they approach the boundary temporarily hold their position before annihilating with pillar-associated −1/2 defects (Fig. 5*J*). While positive defects that directly approach the pillar can temporarily enter the depleted area by driving active material ahead of them, such infrequent events are transient (Movie S8) as the repulsive active force (Fig. 5*C*) pushes such incursions radially outward.

Conclusions

Using a combined experimental and simulation approach, we have demonstrated that micropatterns fully submersed in an underlying oil layer can guide the flow, topology, and even concentration of active material in superjacent nematic films without direct contact. By imposing changes in substrate depth, viscous dissipation in the oil layer enacts a position-dependent effective friction coefficient on the active material. Abrupt substrate height steps can constitute sharp virtual boundaries in the active matter layer, which can control flow and defect behavior. As proof-of-concept systems, we presented virtual channels exhibiting coexisting flow states, sinusoid substrates that gently guide defects, stairways separating active turbulence with dif-

fering characteristic length, and a virtual enclosure depleted of active material that acts as an obstacle scattering nearby defects.

The proposed technique of fully submersed micropatterned structures facilitates approaches for fabricating complex active topological microfluidic devices. For example, complications associated with infiltration of active nematics into confined spaces could be avoided, and active dynamics in various geometries at the same activity could be compared directly. Furthermore, locally concentrating or depleting active material could regulate activity at constant levels of adenosine triphosphate (ATP) or rheological properties such as film viscosity or nematic elastic coefficient through this approach.

Materials and Methods

Formation of the Active Nematic Network. An active nematic microtubule network is generated following the protocol previously reported by Sanchez et al. (59) at an oil–water interface. Prior to experiments, active premixtures are prepared in 3.73-μL aliquots containing biotin-labeled K401 kinesin motors, streptavadin, pyruvate kinase/lactic dehydrogenase (PKLDH), phosphoenol pyruvate (used for ATP regeneration), 4 mg/mL glucose, 0.27 mg/mL glucose oxidase, 47 μg/mL catalase, 2 mM Trolox, and 6%

(wt/vol) 20kDa polyethylene glycol (PEG) in M2b buffer (80 mM piperazine-N,N'-bis(2-ethanesulfonic acid) [Pipes], pH 6.8, 2 mM MgCl$_2$, and 1 mM ethylene glycol-bis(β-aminoethyl ether)-N,N,N',N'-tetraacetic acid [EGTA]). To prevent photobleaching during imaging, premixtures contain 6.65nM dithiothreitol (DTT), an antioxidant solution. After the premix is prepared, the aliquots are flash frozen in liquid nitrogen and promptly stored at −80°C for future use.

To perform active nematic experiments, 1 mM ATP (final concentration) is added to the 3.73-μL premixture aliquot followed by 2 μL of 6 mg/mL (3%) Alexa Fluor 647–labeled guanylyl-(α,β)-methylene-diphosphonate (GMPCPP) microtubules (for a final concentration of 1 mg/mL). For fluorescence imaging, microtubules are fluorescently labeled with Alexa Fluor 647 (59). The result is a suspended active nematic with a total volume of 6 μL. We use an ATP concentration at saturation (i.e., the local microtubule extension speed was maximized). To confine the active nematic at an oil–water interface, we follow the previously published procedure (18, 59). We first create a flow cell made from the glass substrate with patterned structures, double-sided tape, and a coverslip treated with a polyacrylamide brush (Fig. 1). The polyacrylamide brush prevents excess protein binding to the coverslip.

We flow in an oil–surfactant mixture (3M Novec HFE 7500 Engineered Fluid with 1.8% PFPE-PEG-PFPE [perfluoropolyether] surfactant) into the channel. Then, this mixture is exchanged with the active microtubule network. We ensure that the amount of oil in the channel is constant over time after filling by sealing the flow cell after preparation. For filling consistency, each cell is prepared using identical spacers and volumes of oil; however, some variation in oil thickness is expected due to microfabrication tolerances. This system forms a three-dimensional (3D) unconfined active microtubule network. Streptavidin can bind up to four biotin-labeled kinesin molecules, and when microtubules of opposing polarities align parallel to each other, the kinesin molecules oriented at 180° to each other walk in opposite directions along those neighboring microtubules. As the kinesins walk, the filaments produce an extensile motion driven by ATP hydrolysis. The ends of the flow cell are sealed using an ultraviolet (UV)-curable glue (RapidFix). The active layer is then centrifuged using a swinging bucket rotor for 42 min at 300 rpm. The dynamic viscosity of the oil layer is 1.24×10^{-3} Pa · s, and the film viscosity of the active nematic gel has previously been found to be $\sim 10^{-3}$ Pa · s · m (56).

Photolithography. The trench and pillar geometries are produced using photolithography. SU-8 (MicroChem Corp.) is a negative tone epoxy-based photoresist that is used to create thin film plastics on substrates. SU-8 is composed of epoxy-based monomers and photoacid generators (PAGs) suspended in a solvent. Upon exposure to UV light, the PAGs release acids, serving as a catalyst for cross-linking available epoxy groups on the monomer after heat is applied to the substrate. Prior to fabrication, glass substrates are thoroughly cleaned in soap and water followed by 30 min of sonication in acetone, methanol, and ethanol in that order. The glass substrates are rinsed in nanopure water to ensure minimal presence of surface contaminants. The glass is then plasma treated with oxygen for 2 min. To ensure the removal of residual moisture left on the substrate, the glass substrate is placed on a hot plate for 5 min at 200°C; the substrate is left to cool down to room temperature for 5 min in a humidity-controlled environment.

Upon thorough cleaning, a quarter-sized drop of SU-8 50 is deposited on the glass substrate. The SU-8 is spin coated at 2,000 rpm for 45 s followed by a 10-min wait. The substrate is soft baked at 65°C for 12 min and then at 95°C for 45 min on a hot plate to evaporate solvent. The substrate is again left to cool to room temperature with another wait of 10 min. The film is then exposed to 365-nm UV light (500mJ/cm^{-2}) followed by a 10-min wait step. To cross-link the exposed regions' epoxy groups, the substrate undergoes a postexposure bake for 5 min at 65°C and then for 15 min at 95°C on a hot plate. After the 15-min bake, the hot plate is turned off and allowed to cool to room temperature without the removal of the coated substrate. This step is to avoid thermally shocking the film, which can result in cracks and poor adhesion. The substrate is developed for 30 min with gentle agitations. After developed, the residual SU-8 developer is rinsed with isopropanol and deionized water, then, it is dried with nitrogen gas. After development, the substrate is then hard baked for 2 min at 150°C. Internal stresses within the substrate due to the abrupt change in surface height are apparent near the edge of the trench as parallel lines in Fig. 1B. This accounts for the gap in data at the trench edge in Fig. 2C. We note that some local residual SU-8 is present at the base of the pillar in Fig. 1H, but this material does not appear to affect the active nematic flow dynamics. The heights of the microstructures are measured using profilometry.

Micromilling. The stepped substrate and the sinusoid surface are produced using computer numerical-controlled micromilling. We use the milling machine TN5-V8-TC8 (MDA Precision) to fabricate the microstructures from poly(methyl methacrylate), commonly known as acrylic. This milling machine is capable of handling drills and endmills as small as 50 μm in diameter and has a spindle rotational accuracy of around 2 μm. The first designed system has steps (height), each with a rise of $\Delta_s = 10 \pm 1$ μm and a run (horizontal width) of $w_s = 500 \pm 2$ μm. The system is composed of 10 steps. The smaller of the two sinusoid systems has undulations with a peak-to-peak amplitude $\Delta_u = 40 \pm 2$ μm and a wavelength $\lambda_u = 150 \pm 2$ μm, while the larger has a peak-to-peak amplitude $\Delta_u = 50 \pm 2$ μm and a wavelength $\lambda_u = 150 \pm 2$ μm. After milling, these features are used as a mold and transferred into a soft elastomer, polydimethylsiloxane, which in turn, is used as a mold again to transfer the features into a cyclic olefin copolymer (COC) using a thermopress. The COC sheets of thickness ranging from 150 to 350 μm are then immersed for 1 h in a solution of 10 wt % 8-Anilino-1-naphthalenesulfonic acid (ANS), a hydrophobic dye, dissolved in a mixture of 85 wt % ethanol and 15 wt % decalin. This treatment adds a fluorescent layer of ANS dye to the COC surface, which allows us to use a 944 Leica SP8 UV/Visible Laser Confocal Microscope to measure the fluorinated oil's thickness under the active nematic. The confined active nematic is imaged using a wide-field fluorescence Nikon Eclipse Ti-E microscope with an Andor Clara camera controlled by Micromanager open-source software.

Data Processing. To investigate how defect dynamics in the active layer are influenced by submersed structures, labeled microtubule bundles are imaged using fluorescence microscopy. Four hundred–frame videos are collected at 1 frame per second and processed using Fiji/ImageJ version 1.52a software. To acquire defect distributions, active nematic microtubule defects are identified and counted manually every 10 frames for each video. The 2D Cartesian components for both x and y axes are acquired from both +1/2 and −1/2 defects using the Click Coordinates Tool plugin on Fiji/ImageJ. For the submersed trench geometry, we use MATLAB to analyze the frequency and position for both +1/2 and −1/2 defects across the channel. Defects are organized and binned in 10-μm horizontal increments across the field of view.

For the stairway geometry and pillar geometries, we apply the same counting procedure to obtain +1/2 and −1/2 defect positional frequencies across all frames. In the stairway geometry, we apply the counting procedure sequentially to each step, and for the pillar, the videos are processed by centering the pillar in a 400 × 400-μm^2 window. Similar to the analysis done with the submersed trench, we use MATLAB to generate a 2D histogram to represent the frequency of the +1/2 and −1/2 defects, positionally distributed in a 2D plane. Defects are organized and binned every 13.4 μm in both horizontal and vertical increments.

The nematic director field inside the channel was calculated using a Fourier transform–based method reported recently by our group (18). To measure the director orientation directly above trenches, the imaged active nematic is oriented with the long axis parallel to the y axis. Each pixel is converted to micrometers (0.9434 μm per pixel). Each pixel from each frame containing an x component, y component, and angle of the bundled-microtubule director is represented on a 2D grid and determined using MATLAB. Our process uses a nested loop and a conditional statement to determine if the angle is between 80° and 90°; if a director satisfied this condition along the y axis for the specified x position, the total is summed and then divided by the total number of angles checked by the loop. This probability is appended to a new horizontal array for each probability in the x position. The result is a time-averaged director orientation mapped across the trench, averaging over all y values.

Simulations. To complement the experiments, we simulate the active nematic thin film using a 2D hybrid lattice Boltzmann/finite difference approach. The incompressible active nematic film flows with velocity $\boldsymbol{u}(\boldsymbol{r};t)$ have long-range orientational order described by the tensor order parameter $\boldsymbol{Q}(\boldsymbol{r};t)$ and varying concentrations of active material, which we take to be a phase field $\phi(\boldsymbol{r};t)$ varying from zero to one, coarsely describing the local amount of active materials (microtubules, kinesin complexes, and ATP). The total free energy includes nematic bulk (LdG) and deformation (FO) terms as well as a binary mixture bulk (DW) term and an interfacial (I) term; $\mathcal{F}[\boldsymbol{Q}, \phi] = \int d^2\boldsymbol{r} \, (f_{LdG} + f_{FO} + f_{DW} + f_I)$. Four coupled equations describe the time evolution of the continuous fields.

The first is the Beris–Edwards equation for nematics:

$$(\partial_t + \boldsymbol{u} \cdot \boldsymbol{\nabla})\boldsymbol{Q} - \boldsymbol{S} = \Gamma_Q \boldsymbol{H}. \qquad [1]$$

8 of 10 | PNAS
https://doi.org/10.1073/pnas.2106038118

Thijssen et al.
Submersed micropatterned structures control active nematic flow, topology, and concentration

The corotation term $\boldsymbol{S} = (\xi\boldsymbol{D}+\boldsymbol{\Omega})(\boldsymbol{Q}+\frac{1}{3}\boldsymbol{I}) + (\boldsymbol{Q}+\frac{1}{3}\boldsymbol{I})(\xi\boldsymbol{D}-\boldsymbol{\Omega}) - 2\xi(\boldsymbol{Q}+\frac{1}{3}\boldsymbol{I})\mathrm{tr}(\boldsymbol{QW})$ determines the alignment of the microtubules in response to gradients in the velocity field, with $\boldsymbol{\Omega}$ the rotational part, and $\boldsymbol{D}$ is the extensional part of the velocity gradient tensor $\boldsymbol{W} = \nabla\boldsymbol{v} = \boldsymbol{\Omega}+\boldsymbol{D}$. The alignment parameter ξ is taken to be in the flow aligning regime and set to $\xi = 0.5$. The resulting Leslie angle (60, 61) is $\theta_\mathrm{L} = \frac{1}{2}\cos^{-1}\left(\frac{\xi(3S+4)}{9S}\right)$.

The molecular field $\boldsymbol{H} = -(\frac{\delta\mathcal{F}}{\delta\boldsymbol{Q}} - \frac{1}{3}\boldsymbol{I}\mathrm{Tr}\frac{\delta\mathcal{F}}{\delta\boldsymbol{Q}})$ is a functional derivative of free energy density $\mathcal{F}$, describing the relaxation toward equilibrium at a rate Γ_Q. The free energy depends directly on the nematic tensor $\boldsymbol{Q}$ and the active material concentration ϕ. The nematic part consists of a Landau–De Gennes contribution, $f_\mathrm{LdG} = A_0\left\{\frac{1}{2}\left(1-\frac{\nu}{3}\right)\mathrm{tr}\left[\boldsymbol{Q}^2\right] - \frac{\nu}{3}\mathrm{tr}\left[\boldsymbol{Q}^3\right] + \frac{\nu}{4}\mathrm{tr}\left[\boldsymbol{Q}^2\right]^2\right\}$ with $A_0 = 0.05$, and Frank–Oseen deformation $f_\mathrm{FO} = \frac{K}{2}(\nabla\boldsymbol{Q})^2$ with $K = 0.02$. We set $\nu = 2.55$, which favors the isotropic state in the absence of active flows (58) and is independent of $\phi(\boldsymbol{r};t)$. This choice allows nematic ordering only due to activity-induced flows, in agreement with experiments (59) and previous simulations (58, 62). Throughout the simulations, the nematic order S is found to be between 0 and 0.3. For the trench data of Fig. 3C, we find $S = 0.18$ and calculate a Leslie angle of $\theta_\mathrm{L} = 22°$.

The active material concentration evolves according to a Cahn–Hillard model. We assume that the film is incompressible and that active material concentration ϕ does not impact fluid mass density ρ:

$$\partial_t\phi + \nabla\cdot(\boldsymbol{u}\phi) = \Gamma_\phi\nabla^2\mu, \qquad [2]$$

where $\mu = \frac{\delta\mathcal{F}}{\delta\phi} - \nabla\cdot\left(\frac{\delta\mathcal{F}}{\delta\nabla\phi}\right)$ is the chemical potential and $\Gamma_\phi = 0.1$ is a mobility coefficient. The double-well free energy density depends on phase as $f_\mathrm{DW} = \frac{A_\phi}{2}\phi^2(\phi-1)^2$ and an interfacial term $f_\mathrm{I} = \frac{K_\phi}{2}(\nabla\phi)^2$ with $A_\phi = 0.03$ and $K_\phi = 0.1$. The free energy minima are at $\phi = \{0, 1\}$. While positive A_ϕ favors phase separation, activity suppresses demixing, and ϕ does not phase separate into high- and low-ϕ regions for sufficiently active flows. In our model, active flows above high-friction regions (such as within the perimeter of the pillar geometry) can become sufficiently small for spinodal decomposition to occur. This does not happen in the low-friction region. We have verified that depletion in the pillar geometry also occurs for a binary mixture free energy modeled using a single well, which would not thermodynamically phase separate. We initialize the concentration to $\phi = 0.5$. All reported phenomena are due to dynamical interactions since the free energy does not favor global nematic ordering nor phase separation.

Lastly, the system obeys the Navier–Stokes equations for the velocity field within the active film. Assuming constant fluid mass density ρ (not active material concentration ϕ) leads to the incompressibility condition

$$\nabla\cdot\boldsymbol{u} = 0. \qquad [3]$$

Because the experimental active nematic film lies on a 2D interface between two 3D fluids, the planar divergence of the velocity could conceivably be nonzero. However, nonzero divergent velocity fields would require continuous circulation in the thin aqueous/oil layers above/below the film. As we are unaware of evidence indicating such flows, we assume 2D incompressibility, implying divergence-free flow. Since the fluid is taken to be incompressible, any outward fluid mass flux into an enclosed area must be balanced by an inward flux and vice versa. If this constraint is relaxed, we allow flow sources in our film, and nonselective outward pointing forces $\zeta\partial_r S(r;t)\hat{\boldsymbol{r}}$, where the ζ is independent of ϕ, will also deplete the material.

The second equation is the Cauchy momentum equation

$$\rho(\partial_t + \boldsymbol{u}\cdot\nabla)\boldsymbol{u} = -\nabla p + \nabla\cdot\boldsymbol{\Pi} - \gamma\boldsymbol{u}, \qquad [4]$$

where p is the pressure and $\boldsymbol{\Pi}$ is the stress tensor, which includes the standard viscous stress $\boldsymbol{\Pi}^\mathrm{visc} = 2\eta\boldsymbol{E}$ for film viscosity $\eta = 2/3$. Furthermore, it contains the elastic stress due to the nematic nature of the microtubules

$$\boldsymbol{\Pi}^\mathrm{elastic} = 2\xi\mathcal{Q}(\boldsymbol{Q}:\boldsymbol{H}) - \xi\boldsymbol{H}\cdot\mathcal{Q} - \xi\mathcal{Q}\cdot\boldsymbol{H}$$
$$- \nabla\boldsymbol{Q}:\frac{\delta\mathcal{F}}{\delta\nabla\boldsymbol{Q}} + \boldsymbol{Q}\cdot\boldsymbol{H} - \boldsymbol{H}\cdot\boldsymbol{Q}, \qquad [5]$$

where $\mathcal{Q} = \boldsymbol{Q}+\boldsymbol{I}/3$. The stress also contains the capillary stresses $\boldsymbol{\Pi}^\mathrm{cap} = (\mathcal{F} - \mu\phi)\boldsymbol{I} - \nabla\phi\left(\frac{\delta\mathcal{F}}{\delta\nabla\phi}\right)$ due to differences in concentration ϕ, and the active component

$$\boldsymbol{\Pi}^\mathrm{act} = -\zeta(\boldsymbol{r};t)\boldsymbol{Q} = -\zeta_0\phi(\boldsymbol{r};t)\boldsymbol{Q}. \qquad [6]$$

Here, we have taken the local activity

$$\zeta(\boldsymbol{r};t) = \zeta_0\phi(\boldsymbol{r};t) \qquad [7]$$

to scale directly with active material concentration. We set $\zeta_0 = 0.09$. While the velocity and director fields can in principle develop out-of-plane components in the nematic film, in experiments and for the parameter values used in this study, no out-of-plane components develop (44). Comparison with strictly 2D simulations has confirmed the qualitative agreement (63).

In the Navier–Stokes equation, we also include an effective friction $\gamma(\boldsymbol{r})$. Employing an effective friction that varies with oil-layer depth neglects any recirculation effects within the oil layer, which is justified by the facts that the micropatterned structures are characterized by small height/width ratios and that the Reynolds numbers of flows within the oil layers are infinitesimal. Hence, typical recirculation vortices around pillars are neglectable (64). Since previous studies have successfully modeled the dynamics of microtubule/kinesin-based active nematic films with weak effective friction (65), we treat the friction as negligible in the regions of the film superjacent to deep structures. In the regions above shallows, we include lubrication momentum dissipation via a nonzero effective friction coefficient. We set $\gamma(h_s) = 0.07$ in the shallows for simulations of the trench system. We define a characteristic confinement scale to be $R \equiv 20$ lattice Boltzmann (LB) nodes. This is comparable with the intrinsic active nematic length scale, and as a result, the reported defect densities are of order unity. The narrowest trench width is $w_t = 1.2R$ (Fig. 3C), and the two wider trenches have widths of $w_t = 1.7R$ (Fig. 3B) and $6R$ (Fig. 3D). All trenches are simulated in $7.5R \times 30R$ periodic systems. For the stairway, we simulate a $7.5R \times 50R$ long system composed of the same number of steps as in the experimental system (10 steps) of width $w_s = 5R$. Each step represents a different lubrication momentum dissipation region with different nonzero effective friction coefficients set to $\gamma(h_s, n) = \frac{0.1}{1+n}$, where $n \in \{0\dots9\}$ denotes the different steps corresponding to different oil depths in the experiments. In the text, we present simulation results from steps $n = \{1, 2, 3, 4, 5\}$. For the pillars, we use a radius $r_p = R$. The friction coefficient is chosen to be sufficiently large to clearly match the pronounced depletion observed experimentally in Fig. 5. We present results for the value $\gamma(h_p) = 0.5$ but observe depletion of ϕ for $\gamma(h_s) = 0.07$, corresponding to the choice used for the trench geometry. The pillar is simulated in a $10R \times 10R$ periodic system.

Defects are detected by calculating the winding number (66). If the average nematic order S in a range of three LB nodes around a defect is lower than 0.05, we assign this defect to be virtual and ignore it.

Data Availability. All study data are included in the article and/or supporting information.

1. D. Dell'Arciprete et al., A growing bacterial colony in two dimensions as an active nematic. Nat. Commun. 9, 4190 (2018).

2. Z. You, D. J. G. Pearce, A. Sengupta, L. Giomi, Geometry and mechanics of microdomains in growing bacterial colonies. Phys. Rev. X 8, 031065 (2018).

3. H. Li et al., Data-driven quantitative modeling of bacterial active nematics. Proc. Natl. Acad. Sci. U.S.A. 116, 777–785 (2019).

4. D. van Holthe tot Echten, G. Nordemann, M. Wehrens, S. Tans, T. Idema, Defect dynamics in growing bacterial colonies. arXiv [Preprint] (2020). https://arxiv.org/abs/2003.10509 (Accessed 31 August 2021).

5. G. Duclos, C. Erlenkämper, J. Joanny, P. Silberzan, Topological defects in confined populations of spindle-shaped cells. Nat. Phys. 13, 58–62 (2017).

6. T. B. Saw et al., Topological defects in epithelia govern cell death and extrusion. Nature 544, 212–216 (2017).

Thijssen et al.
Submersed micropatterned structures control active nematic flow, topology, and concentration

PNAS | 9 of 10
https://doi.org/10.1073/pnas.2106038118

7. K. Kawaguchi, R. Kageyama, M. Sano, Topological defects control collective dynamics in neural progenitor cell cultures. *Nature* **545**, 327–331 (2017).
8. G. Duclos *et al*., Spontaneous shear flow in confined cellular nematics. *Nat. Phys.* **14**, 728–732 (2018).
9. C. Pérez-González *et al*., Active wetting of epithelial tissues. *Nat. Phys.* **15**, 79–88 (2019).
10. R. Zhang, N. Kumar, J. L. Ross, M. L. Gardel, J. J. de Pablo, Interplay of structure, elasticity, and dynamics in actin-based nematic materials. *Proc. Natl. Acad. Sci. U.S.A.* **115**, E124–E133 (2018).
11. L. Huber, R. Suzuki, T. Krüger, E. Frey, A. R. Bausch, Emergence of coexisting ordered states in active matter systems. *Science* **361**, 255–258 (2018).
12. N. Kumar, R. Zhang, J. J. de Pablo, M. L. Gardel, Tunable structure and dynamics of active liquid crystals. *Sci. Adv.* **4**, eaat7779 (2018).
13. M. M. Norton *et al*., Insensitivity of active nematic liquid crystal dynamics to topological constraints. *Phys. Rev. E* **97**, 012702 (2018).
14. A. Opathalage *et al*., Self-organized dynamics and the transition to turbulence of confined active nematics. *Proc. Natl. Acad. Sci. U.S.A.* **116**, 4788–4797 (2019).
15. J. Hardoüin, J. Laurent, T. Lopez-Leon, J. Ignés-Mullol, F. Sagués, Active microfluidic transport in two-dimensional handlebodies. *Soft Matter* **16**, 9230–9241 (2020).
16. H. Reinken *et al*., Organizing bacterial vortex lattices by periodic obstacle arrays. *Commun. Phys.* **3**, 1–9 (2020).
17. B. Zhang, B. Hilton, C. Short, A. Souslov, A. Snezhko, Oscillatory chiral flows in confined active fluids with obstacles. *Phys. Rev. Res.* **2**, 043225 (2020).
18. A. J. Tan *et al*., Topological chaos in active nematics. *Nat. Phys.* **15**, 1033–1039 (2019).
19. E. Bertin, A. Baskaran, H. Chaté, M. C. Marchetti, Comparison between Smoluchowski and Boltzmann approaches for self-propelled rods. *Phys. Rev. E Stat. Nonlin. Soft Matter Phys.* **92**, 042141 (2015).
20. A. M. Nagel, M. Greenberg, T. N. Shendruk, H. W. de Haan, Collective dynamics of model pili-based twitcher-mode bacilliforms. *Sci. Rep.* **10**, 10747 (2020).
21. M. Bär, R. Großmann, S. Heidenreich, F. Peruani, Self-propelled rods: Insights and perspectives for active matter. *Annu. Rev. Condens. Matter Phys.* **11**, 441–466 (2020).
22. M. N. van der Linden, L. C. Alexander, D. G. A. L. Aarts, O. Dauchot, Interrupted motility induced phase separation in aligning active colloids. *Phys. Rev. Lett.* **123**, 098001 (2019).
23. L. Caprini, U. Marini Bettolo Marconi, A. Puglisi, Spontaneous velocity alignment in motility-induced phase separation. *Phys. Rev. Lett.* **124**, 078001 (2020).
24. R. Großmann, I. S. Aranson, F. Peruani, A particle-field approach bridges phase separation and collective motion in active matter. *Nat. Commun.* **11**, 5365 (2020).
25. G. Mahmud *et al*., Directing cell motions on micropatterned ratchets. *Nat. Phys.* **5**, 606–612 (2009).
26. J. Katuri, D. Caballero, R. Voituriez, J. Samitier, S. Sanchez, Directed flow of micromotors through alignment interactions with micropatterned ratchets. *ACS Nano* **12**, 7282–7291 (2018).
27. L. Angelani, R. Di Leonardo, G. Ruocco, Self-starting micromotors in a bacterial bath. *Phys. Rev. Lett.* **102**, 048104 (2009).
28. A. Sokolov, M. M. Apodaca, B. A. Grzybowski, I. S. Aranson, Swimming bacteria power microscopic gears. *Proc. Natl. Acad. Sci. U.S.A.* **107**, 969–974 (2010).
29. P. Pietzonka, E. Fodor, C. Lohrmann, M. E. Cates, U. Seifert, Autonomous engines driven by active matter: Energetics and design principles. *Phys. Rev. X* **9**, 041032 (2019).
30. R. Sunyer, X. Trepat, Durotaxis. *Curr. Biol.* **30**, R383–R387 (2020).
31. E. A. Novikova, M. Raab, D. E. Discher, C. Storm, Persistence-driven durotaxis: Generic, directed motility in rigidity gradients. *Phys. Rev. Lett.* **118**, 078103 (2017).
32. K. Schakenraad *et al*., Topotaxis of active Brownian particles. *Phys. Rev. E* **101**, 032602 (2020).
33. A. Sokolov, A. Mozaffari, R. Zhang, J. J. de Pablo, A. Snezhko, Emergence of radial tree of bend stripes in active nematics. *Phys. Rev. X* **9**, 031014 (2019).
34. M. M. Norton, P. Grover, M. F. Hagan, S. Fraden, Optimal control of active nematics. *Phys. Rev. Lett.* **125**, 178005 (2020).
35. D. P. Rivas, T. N. Shendruk, R. R. Henry, D. H. Reich, R. L. Leheny, Driven topological transitions in active nematic films. *Soft Matter* **16**, 9331–9338 (2020).
36. P. W. Ellis *et al*., Curvature-induced defect unbinding and dynamics in active nematic toroids. *Nat. Phys.* **14**, 85–90 (2018).
37. D. J. G. Pearce, P. W. Ellis, A. Fernandez-Nieves, L. Giomi, Geometrical control of active turbulence in curved topographies. *Phys. Rev. Lett.* **122**, 168002 (2019).
38. R. Zhang *et al*., Spatiotemporal control of liquid crystal structure and dynamics through activity patterning. *Nat. Mater.* **20**, 875–882 (2021).
39. S. Shankar, M. C. Marchetti, Hydrodynamics of active defects: From order to chaos to defect ordering. *Phys. Rev. X* **9**, 041047 (2019).
40. X. Tang, J. V. Selinger, Alignment of a topological defect by an activity gradient. *Phys. Rev. E* **103**, 022703 (2021).
41. A. Mozaffari, R. Zhang, N. Atzin, J. J. de Pablo, Defect spirograph: Dynamical behavior of defects in spatially patterned active nematics. *Phys. Rev. Lett.* **126**, 227801 (2021).
42. P. Guillamat, J. Ignés-Mullol, F. Sagués, Taming active turbulence with patterned soft interfaces. *Nat. Commun.* **8**, 564 (2017).
43. T. N. Shendruk, A. Doostmohammadi, K. Thijssen, J. M. Yeomans, Dancing disclinations in confined active nematics. *Soft Matter* **13**, 3853–3862 (2017).
44. A. Doostmohammadi, T. N. Shendruk, K. Thijssen, J. M. Yeomans, Onset of meso-scale turbulence in active nematics. *Nat. Commun.* **8**, 15326 (2017).
45. S. Chandragiri, A. Doostmohammadi, J. M. Yeomans, S. P. Thampi, Active transport in a channel: Stabilisation by flow or thermodynamics. *Soft Matter* **15**, 1597–1604 (2019).
46. J. Hardoüin *et al*., Reconfigurable flows and defect landscape of confined active nematics. *Commun. Phys.* **2**, 1–9 (2019).
47. L. M. Pismen, F. Sagués, Viscous dissipation and dynamics of defects in an active nematic interface*. *Eur Phys J E Soft Matter* **40**, 92 (2017).
48. L. Metselaar *et al*., Electric-field-induced shape transition of nematic tactoids. *Phys. Rev. E* **96**, 022706 (2017).
49. R. Alert, J. F. Joanny, J. Casademunt, Universal scaling of active nematic turbulence. *Nat. Phys.* **16**, 682–688 (2020).
50. K. Thijssen, M. R. Nejad, J. M. Yeomans, Role of friction in multidefect ordering. *Phys. Rev. Lett.* **125**, 218004 (2020).
51. F. Kempf, R. Mueller, E. Frey, J. M. Yeomans, A. Doostmohammadi, Active matter invasion. *Soft Matter* **15**, 7538–7546 (2019).
52. P. Guillamat, J. Ignés-Mullol, F. Sagués, Control of active liquid crystals with a magnetic field. *Proc. Natl. Acad. Sci. U.S.A.* **113**, 5498–5502 (2016).
53. R. Aditi Simha, S. Ramaswamy, Hydrodynamic fluctuations and instabilities in ordered suspensions of self-propelled particles. *Phys. Rev. Lett.* **89**, 058101 (2002).
54. L. Giomi, L. Mahadevan, B. Chakraborty, M. F. Hagan, Excitable patterns in active nematics. *Phys. Rev. Lett.* **106**, 218101 (2011).
55. B. Martínez-Prat, J. Ignés-Mullol, J. Casademunt, F. Sagués, Selection mechanism at the onset of active turbulence. *Nat. Phys.* **15**, 362–366 (2019).
56. P. Guillamat, J. Ignés-Mullol, S. Shankar, M. C. Marchetti, F. Sagués, Probing the shear viscosity of an active nematic film. *Phys. Rev. E* **94**, 060602 (2016).
57. B. Martínez-Prat *et al*., Scaling regimes of active turbulence with external dissipation. arXiv [Preprint] (2021). https://arxiv.org/abs/2101.11570 (Accessed 31 August 2021).
58. S. P. Thampi, A. Doostmohammadi, R. Golestanian, J. M. Yeomans, Intrinsic free energy in active nematics. *Europhys. Lett.* **112**, 28004 (2015).
59. T. Sanchez, D. T. N. Chen, S. J. DeCamp, M. Heymann, Z. Dogic, Spontaneous motion in hierarchically assembled active matter. *Nature* **491**, 431–434 (2012).
60. K. Thijssen, L. Metselaar, J. M. Yeomans, A. Doostmohammadi, Active nematics with anisotropic friction: The decisive role of the flow aligning parameter. *Soft Matter* **16**, 2065–2074 (2020).
61. K. Thijssen, A. Doostmohammadi, Binding self-propelled topological defects in active turbulence. *Phys. Rev. Res.* **2**, 042008(R) (2020).
62. P. Srivastava, P. Mishra, M. C. Marchetti, Negative stiffness and modulated states in active nematics. *Soft Matter* **12**, 8214–8225 (2016).
63. E. J. Hemingway, P. Mishra, M. C. Marchetti, S. M. Fielding, Correlation lengths in hydrodynamic models of active nematics. *Soft Matter* **12**, 7943–7952 (2016).
64. C. Baykal, B. M. Sumer, D. R. Fuhrman, N. G. Jacobsen, J. Fredsøe, Numerical investigation of flow and scour around a vertical circular cylinder. *Philos. Trans. A Math. Phys. Eng. Sci.* **373**, 20140104 (2015).
65. Z. Zhou *et al*., Machine learning forecasting of active nematics. *Soft Matter* **17**, 738–747 (2021).
66. J. Hobdell, A. Windle, A numerical technique for predicting microstructure in liquid crystalline polymers. *Liq. Cryst.* **23**, 157–173 (1997).